Quadrupole collectivity in the two-body random ensemble

Volha Abramkina and Alexander Volya

Quadrupole collectivity in the two-body random ensemble

Volha Abramkina and Alexander Volya

Department of Physics, Florida State University, Tallahassee, FL 32306-4450, USA

(Dated: July 6, 2011)

We conduct a systematic investigation of the nuclear collective dynamics that emerges in systems with two-body random interactions. We explore the development of the mean field and study its geometry. We investigate multipole collectivities in the many-body spectra and their dependence on the underlying two-body interaction Hamiltonian. The quadrupole-quadrupole interaction component appears to be dynamically dominating in the two-body random ensemble. This quadrupole coherence leads to rotational spectral features and thus suggests the formation of the deformed mean-field of a specific geometry.

I. INTRODUCTION

Emergent phenomena are one of the most profound topics in modern science, addressing the ways that collectivities and complex patterns appear due to multiplicity of components and simple interactions. Ensembles of random Hamiltonians allow one to explore the emergent phenomena in a statistical way, and thus to establish generic relations and rules. To study the many-body physics of interest, we adopt a shell model approach with a two-body interaction Hamiltonian. The sets of the two-body interaction strengths are selected at random, resulting in the two-body random ensemble (TBRE) [1]. Symmetries, such as rotational, isospin, and parity, entangled with complex many-body dynamics result in surprising regularities discovered recently in the low-lying spectrum. Patterns exhibited by the random ensembles are remarkably similar to those observed in real nuclei. The high probability for the ground state spin to be zero is the most astounding feature of the TBRE discovered in Ref. [1]. Signs of almost every collective feature seen in nuclei, namely, pairing superconductivity, deformation, and vibration, have been observed in the TBRE [2–6]. While the systematics of the ground state quantum numbers is almost not sensitive to the short-range pairing matrix elements, the probability to find a coherent paired structure in the wave-functions of low-lying states is enhanced [2]. The presence of rotational characteristics in the spectra is another unexpected result seen in the TBRE [2, 7].

The goal of this work is to study the emergence of collective mean-field dynamics in ensembles with random interactions. The discussion is organized as follows: In Sec. II we briefly define the TBRE, introduce signatures of collective motion, and discuss ways to detect them. In Sec. III we present our study of collectivities in single-j level models. More complex models are explored in Secs. IV and V. We summarize our results in Sec VI with a discussion of the quadrupole-quadrupole Hamiltonian which appears to be responsible for most of the observed phenomena.

II. COLLECTIVE OBSERVABLES AND MODELS

In the spirit of the traditional shell model approach, we define a model configuration as $(j_1, j_2 \ldots)^N$, where N nucleons occupy a set of single-particle levels labeled by their angular momentum j. In this work, unless explicitly stated otherwise, the single-particle energies are degenerate. The Hamiltonians in the TBRE are defined with a set of two-body matrix elements which are selected at random. The distribution of the two-body matrix elements is Gaussian so that, within a given symmetry class, the ensemble of Hamiltonian matrices for two particles coincides with Gaussian Orthogonal Ensemble. The presence of rotational symmetry and, where relevant, of parity and isospin symmetries is assumed. The distribution variances are selected to be the same for all symmetry classes. The typical number of random realizations is between 10^5 and 10^7 for all ensembles presented in this work.

In the TBRE the number of realizations with the ground state spin $J_{gs} = 0$ is disproportionally large. Aiming at collective phenomena we select realizations with $J_{gs} = 0$. With the exception of the ground state, labeled as 0_{gs}, we denote the low-lying states by the value of their spin with an identifying subscript. The subscript is given in bold font if it refers to the absolute order of a given state in the spectrum. Throughout this paper we give probabilities of finding realizations with certain features; these probabilities are always quoted as a percentage relative to the size of the ensemble; however, all probability distribution plots are normalized to unit area.

In order to identify and to analyze manifestations of collective phenomena in the spectra we use a set of observables. The goal is to choose a finite number of spectral observables that are likely to convey most of the information about possible collective structures in a scale-independent way and with minimal model dependence. These quantities and the logic behind their selection are discussed in what follows.

The geometry of the nuclear mean field is described by the multipole density operators $\mathcal{M}_{\lambda\mu}$ with multipolarity λ and magnetic component μ. The structure of the mul-

tipole operators depends on the valence space, for each model it is addressed separately. The reduced transition rate from an initial state $|JM\rangle$ to a final state $|J'M'\rangle$

$$B(E\lambda, J \to J') = \frac{1}{2J+1} \sum_{\mu,M,M'} |\langle J'M'|\mathcal{M}_{\lambda\mu}|JM\rangle|^2 \tag{1}$$

is one of the observables. Here $|JM\rangle$ denotes a many-body state with angular momentum J and magnetic projection M. The total transition strength from a state J is given by the sum rule

$$S_\lambda(J) = \sum_{J'} B(E\lambda, J \to J') = \langle JM| \sum_\mu \mathcal{M}^\dagger_{\lambda\mu} \mathcal{M}_{\lambda\mu}|JM\rangle, \tag{2}$$

which provides a convenient normalization to assess the *fractional collectivity* of the transition

$$b(E\lambda, J \to J') = \frac{B(E\lambda, J \to J')}{S_\lambda(J)}. \tag{3}$$

The shape of a state is described by its multipole moments specified by the expectation value

$$\mathcal{Q}_\lambda(J) = \langle JJ|\mathcal{M}_{\lambda 0}|JJ\rangle. \tag{4}$$

For a non-spherical system this moment describes the shape of a deformed nucleus measured in the lab frame. The intrinsic shape is characterized by the body-fixed (intrinsic) multipole moments Q_λ. A rotational spectrum (band) emerges for every fixed intrinsic shape. In a rigid rotor these intrinsic moments are the same for all states in the band and they determine the lab-frame observables in Eqs. (1) and (4). For the ground state band of interest, the intrinsic moments determine the total transition strength $S_\lambda(0_{gs}) = Q_\lambda^2$.

In the axially symmetric case the quantum number K, a projection of the angular momentum onto the body-fixed symmetry axis, is conserved. Then for each rotational K-band the relations between the observables in the lab frame and in the intrinsic frame are expressed via Clebsch-Gordan coefficients $\mathcal{Q}_\lambda(J) = Q_\lambda C^{JJ}_{\lambda 0, JJ} C^{JK}_{\lambda 0, JK}$ and $B(E\lambda, J \to J') = Q_\lambda^2 \left| C^{J'K}_{\lambda 0, JK} \right|^2$. This limit of an axially symmetric rotor provides a suitable normalization of the multipole moments. In this work instead of $\mathcal{Q}_\lambda(J)$ we quote a normalized intrinsic moment

$$q_\lambda(J) = \frac{Q_\lambda(J)}{\sqrt{S_\lambda(0_{gs})}}, \text{ where } Q_\lambda(J) = \frac{\mathcal{Q}_\lambda(J)}{C^{JJ}_{\lambda 0, JJ} C^{J0}_{\lambda 0, J0}}, \tag{5}$$

which is computed as if the state is a member of the $K = 0$ rotational ground state band.

In this paper we only briefly touch on the subject of collectivities other than quadrupole, see Sec. III C; thus for convenience the subscript λ is omitted for $\lambda = 2$. The relation between the lab-frame moment of the 2_1 state and its intrinsic moment is $\mathcal{Q}(2_1) = -2/7\, Q(2_1)$. For an axially symmetric rotor the quadrupole transition sum

rule for the 0_{gs} state is saturated by a single transition $b(E2, 0_{gs} \to 2_1) = 1$. In this case the quadrupole moment is $q(2_1) = 1$ for prolate or $q(2_1) = -1$ for oblate shapes.

We normalize the total transition strength $S_\lambda(J)$ to its maximum possible value for a given valence space. Taking the $\lambda = 2$ case as an example, we define the quadrupole-quadrupole (QQ) Hamiltonian as

$$H_{\text{QQ}} = -\sum_\mu \mathcal{M}^\dagger_{2\mu} \mathcal{M}_{2\mu}. \tag{6}$$

The eigenstate energy of the QQ Hamiltonian coincides with the total transition strength (2) for that state: $E_{\text{QQ}}(J) = -S(J)$. Thus, the absolute value of the ground state energy of the QQ Hamiltonian $|E_{\text{QQ}}(0_{gs})|$ is the maximum possible value of the total transition strength $S(J)$ for a given model space and for a given structure of the quadrupole operator. We therefore define a *relative transition strength* as

$$s(J) = \frac{S(J)}{|E_{\text{QQ}}(0_{gs})|}. \tag{7}$$

To summarize, in our study we use the dimensionless variables defined in Eqs. (3), (5), and (7). To shorten the notation we define $b \equiv b(E2, 0_{gs} \to 2_1)$, $q \equiv q(2_1)$, and $s \equiv s(0_{gs})$. For collective models of pairing, rotations, and vibrations $b \approx 1$. We refer to a realization with $b > 0.7$ as *collective* and with $b < 0.3$ as *non-collective*. The quadrupole moment q allows one to separate different collective modes: $q \approx \pm 1$ for rotations and $q \approx 0$ for vibrations and for paired states. In what follows we allude to collective realizations with $q > 0.7$ as *prolate* and those with $q < -0.7$ as *oblate*. For rotations the relative transition strength s is proportional to the square of the intrinsic moment, and thus it is associated with the Hill-Wheeler deformation parameter β^2. Within Elliot's SU(3) model [8] the relative transition strength s can be thought to represent the expectation value of the Casimir operator which identifies the irreducible representation. In cases where $s \approx 1$ the ground state band structure is close to that of the QQ Hamiltonian.

The collective structure is further analyzed using the following 4_1 state. The types of collective modes can be classified by the ratio of the excitation energies measured relative to the energy of the 0_{gs} state

$$R_{42} = \frac{E(4_1)}{E(2_1)}. \tag{8}$$

This ratio is close to 0 for pairing, 2 for vibration, and 10/3 for rotation. The ratio of deexcitation rates

$$B_{42} = \frac{B(E2, 4_1 \to 2_1)}{B(E2, 2_1 \to 0_{gs})} \tag{9}$$

is another measure. It is nearly 0 for pairing, 2 for vibrational mode, and 10/7 for rotational motion. Typically, for models with the QQ Hamiltonian R_{42} and B_{42} are close to the rotational values, see summary in Tab. I.

A comprehensive review of different collective models, their analytic predictions, and comparisons with rotational spectra observed in real nuclei can be found in the textbooks [9, 10].

III. THE SINGLE j LEVEL MODEL

A. Quadrupole collectivity

We begin our presentation with single j level models. Starting from the original paper [1] the single j level with identical nucleons has been at the center of numerous investigations; a good summary may be found in the following reviews [2, 4, 5, 11]. With many issues understood and with still unanswered questions, the single j model remains an important exploratory benchmark. The model, while simple, has a number of particularly attractive features which can be of both advantage and disadvantage [12]: the Hamiltonian is defined with a small number of parameters; apart from an overall normalization constant, the multipole operators are uniquely defined; a special role is played by the quasispin SU(2) group; and the particle-hole symmetry is exact.

In Fig. 1 the system with 6 nucleons in a single $j = 19/2$ level is examined; we refer to this system as $(19/2)^6$. Here we select the 10.4% of random realizations where the 0_{gs} state is followed by the 2_1 state. The distribution of the fractional collectivity $b \equiv b(E2, 0_{gs} \rightarrow 2_1)$ in Fig. 1(a) points to highly collective nature of the quadrupole transition $0_{gs} \rightarrow 2_1$. Most realizations with 0_{gs} and 2_1 are collective ($b > 0.7$), their fraction is 7.8% of the total number of samples. These realizations are shaded in red. This collectivity is not a statistical coincidence. The system $(19/2)^6$ has 1242 spin-states, among them there are 10 states with $J = 0$ and 23 states with $J = 2$. Thus, the probability for the $0_{gs}, 2_1$ spin sequence to occur among all other possible outcomes is only 0.015%. The large fractional collectivity for the transition between these two states is even more unlikely statistically. The probability of $b(E2, 0_{gs} \rightarrow 2_1) > 0.7$ is of the order of 10^{-7} because the transition strength is shared among 23 $J = 2$ states.

There are two peaks in the distribution of the quadrupole moment in Fig. 1(b), they reflect prolate and oblate deformations. For most of the collective realizations, which are shaded in Fig. 1, the magnitude of the quadrupole moment is consistent with the value for the axially deformed rigid rotor ($|q| \approx 1$). The ground state is most likely to be oblate, but in about one out of four collective cases a prolate mean field emerges.

The collective realizations are further analyzed in Fig. 2 which shows the distribution of the relative transition strength s. In Fig. 2 the oblate ($q < -0.7$) and prolate ($q > 0.7$) cases are shaded with different patterns. The relative transition rate s for the oblate samples is close to the maximum possible value $s = 1$. Thus, for these realizations the ground state band structure is similar
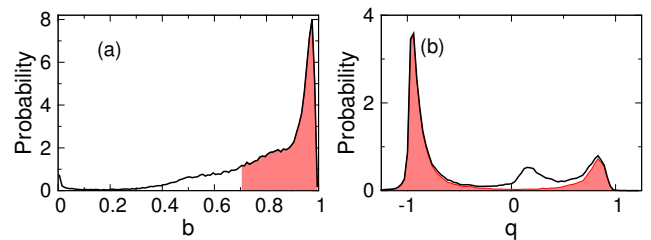

Figure 1: (Color online) $(19/2)^6$. (a) The distribution of the fractional collectivity b. (b) The distribution the intrinsic quadrupole moment q. Only realizations with the $0_{gs}, 2_1$ spin sequence are included in both panels. There are 10.4% of such realizations. The 7.8% of collective realizations ($b > 0.7$) are shaded.

to that of the QQ Hamiltonian. The data on the QQ Hamiltonian for our models is summarized in Sec. VI. For prolate systems the distribution of the relative transition strength peaks around $s = 0.37$.

In Fig. 3 we focus on distributions of the deexcitation ratio B_{42} and the energy ratio R_{24} defined in Eqs. 9 and 8. We use the same shading for prolate and oblate realizations as in Fig. 2, but slightly modify our selection of samples. We chose the collective realizations that have states 2_1 and 4_1, with 2_1 being not higher than the forth excited state and 4_1 being above it.

The collective oblate realizations comprise a peak in the distribution of B_{42} in Fig. 3(a) around the rotational limit of $B_{42} = 10/7 \approx 1.4$. For prolate realizations the distribution peaks near $B_{42} = 0.8$ and has an extended shoulder. It is likely that the rotational structure is fragmented in instances with a weak prolate deformation suggested by the lower values of s seen in Fig. 2. Therefore, the 4_1 state is not purely rotational.

The distribution of the ratio of the excitation energies R_{42} in Fig. 3(b) seems to contradict the rotational limit. For most of the collective realizations the values of the ratio fall between the pairing limit of 1 and the vibrational limit of 2, while in the rotational limit the ratio of 3.3 is expected. This discrepancy has been reconciled in Ref. [1] with the observation that the rotational ordering emerges for the ensemble-averaged excitation energies. The same conclusion is expected from the geometrical chaoticity arguments [13]. Excitation energies are sensitive to non-collective features, this leads to large fluctuations of R_{42}. The experimental observations of realistic nuclei also show that when the quadrupole transition rates follow the rotational systematics, the excitation energy spectrum can deviate from rotational; on occasions, the spectrum is closer to the vibrational limit [9]. The coexistence of both prolate and oblate configurations in this $(19/2)^6$ system could be another reason for the distortion in the energy spectrum. Within Elliot's SU(3) model analogous mixing of group representations was investigated in Ref. [14].
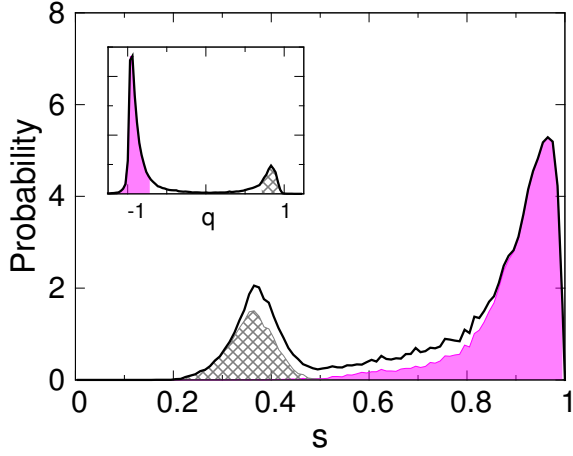
Figure 2: (Color online) $(19/2)^6$. The distribution of the relative transition strength s for the collective realizations (shaded area in Fig. 1). The quadrupole moments shown in the inset are separated into prolate ($q > 0.7$) and oblate ($q < -0.7$) shapes. The resulting distributions are shaded with a pattern and a uniform color, respectively. The fraction of oblate cases is 5.2% and the fraction of prolate cases is 1.3% relative to the total number of random realizations.
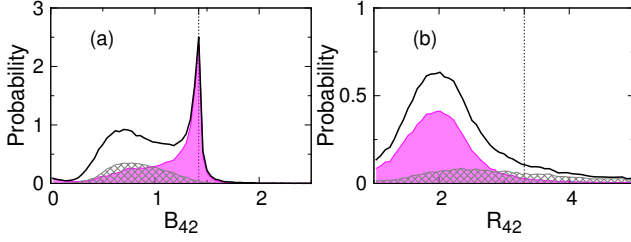

Figure 3: (Color online) $(19/2)^6$. (a) The distribution of the deexcitation ratio B_{42} defined in Eq. (9). (b) The distribution of the excitation energy ratio R_{42} defined in Eq. (8). The distributions are comprised of 13.6% of realizations that have the 0_{gs}, 2_1, 4_1 sequence with $b > 0.7$, the 2_1 state is not higher than the fourth excited state, and $E(4_1) > E(2_1)$. The prolate and oblate cases, which appear in the ensemble with probabilities 3.3% and 7.1% respectively, are shaded with the same patterns as in Fig. 2. The values of B_{42} and R_{42} for the QQ Hamiltonian listed in Tab. I are marked with the vertical grid lines.

B. Triaxiality

The triaxiality is marked by the presence of low-lying levels 2_2, 3_1, 4_2, 5_1. The excitation energies are subject to the equalities $E(2_1) + E(2_2) = E(3_1)$ and $4E(2_1) + E(2_2) = E(5_1)$. It is remarkable that these relations appear to be well satisfied by the spectrum of the QQ Hamiltonian in the $(19/2)^6$ configuration, for which $R_{2_1 3_1} + R_{2_2 3_1} = 1.005$ and $4R_{2_1 5_1} + R_{2_2 5_1} = 1.026$. Here $R_{JJ'} = E(J)/E(J')$ denotes the ratio of excitation energies. The rigid rotor Hamiltonian, defined by three moments of inertia, is responsible for these correlations

in the spectrum.

In this work we examine two low-lying 2_1 and 2_2 states. These are the only states with spin 2 in the triaxial rotor model, they are mixed configurations of $K = 0$ and $K = 2$. We use angle Γ to express the level of the K-mixing. This angle is determined by the three reciprocal moments of inertia A_i, $i = 1, 2, 3$ in the rotor Hamiltonian

$$\tan 2\Gamma = \frac{\sqrt{3}(A_1 - A_2)}{A_1 + A_2 - 2A_3}.$$

The ratio of the excitation energies of the 2_1 and 2_2 states is another parameter of the rotor Hamiltonian. It is convenient to express this ratio $R_{2_1 2_2}$ in terms of the angle γ_{DF} defined using the Davydov-Filippov model of irrotational flow [15] as

$$\sin^2(3\gamma_{DF}) = \frac{9}{2} \frac{R_{2_1 2_2}}{(1 + R_{2_1 2_2})^2}. \tag{10}$$

In our example that follows, the triaxiality is small and $\gamma_{DF}^2 \approx 0.5 R_{2_1 2_2}$. Thus, the rotor Hamiltonian, given by the three moments of inertia, can be equivalently described by an overall energy scale, the K-mixing angle Γ, and the angle γ_{DF}.

The quadrupole shape is parametrized by the Hill-Wheeler parameters β and γ which define the quadrupole operator $\mathcal{M}_{2\mu}$. The relation between the parameters of the rotor Hamiltonian and the intrinsic shape is model-dependent. The irrotational-flow moments of inertia discussed in Ref. [15] result in $\gamma_{DF} = \gamma$ and $\Gamma = \{\arccot[3\cot(3\gamma)] - \gamma\}/2$; the latter implies $\Gamma \ll \gamma$ for small triaxiality. A rather different result follows from the rigid-body moments of inertia.

We determine Γ, γ_{DF}, and γ independently from the spectroscopic observables. The parameter γ_{DF} is obtained from the energy spectrum, Eq. (10). Following Ref. [16] one can view the sum rules

$$b(E2, 0_{gs} \to 2_1) + b(E2, 0_{gs} \to 2_2) = 1$$

and

$$\frac{7}{2} b(E2, 2_1 \to 2_2) + q^2(2_1) = 1$$

for the $J = 2$ two-state model as the Pythagorean theorem for amplitudes. The angles in the corresponding right-angled triangles are $\gamma - \Gamma$ and $\gamma + 2\Gamma$, therefore

$$\tan^2(\gamma - \Gamma) = \frac{B(E2, 0 \to 2_2)}{B(E2, 0 \to 2_1)}, \tag{11}$$

$$\tan^2(\gamma + 2\Gamma) = \frac{2B(E2, 2_1 \to 2_2)}{7Q^2(2_1)}. \tag{12}$$

These equations allow one to determine the triaxiality γ and the K-mixing angle Γ.

All three angles γ, Γ, and γ_{DF} are small in our models with the QQ Hamiltonian, see discussion in Sec. VI.

Correspondingly, in the TBRE the effects of triaxiality are weak but detectable.

For our studies of triaxiality presented in Fig. 4 we use the $(19/2)^6$ model. We recall that in the triaxial rotor model there is a second $J = 2$ state, 2_2, with $\mathcal{Q}(2_1) = -\mathcal{Q}(2_2)$. Thus, we select collective realizations with 0_{gs} and 2_1, and in addition to that we require that in the entire spectrum there is a 2_2 state for which the equality $\mathcal{Q}(2_2) = -\mathcal{Q}(2_1)$ holds within 20% of accuracy. In collective realizations of rotational type the magnitude of the $Q(2_2)$ is large as compared to the quadrupole moments of other many-body states. This simplifies the identification of the 2_2 state. We find that practically for all collective realizations this second 2_2 state exists. Indeed, from the total number of random realizations a large fraction, 18.3%, satisfy all of the mentioned triaxiality conditions. In Figs. 4(a), 4(b), and 4(c) we show the distributions of the triaxiality angle γ, K-mixing angle Γ, and γ_{DF}, respectively. We use the same shading as in Fig. 3 to separate prolate and oblate shapes.

In the $(19/2)^6$ model one often finds collective realizations with oblate intrinsic deformation and $s \approx 1$, these realizations are triaxial with $\gamma \approx 9°$, Fig. 4(a). This result, as well as $\Gamma \approx 0°$ in Fig. 4(b), is consistent with that of the QQ Hamiltonian, see Tab. I. The less frequent prolate cases are nearly axially symmetric.

In the TBRE the angle γ_{DF}, Fig. 4(c), appears on average to be higher than the corresponding angle in the QQ Hamiltonian. The peak in the γ_{DF} distribution is also higher than the peak in the γ distribution, compare Figs. 4(a) and 4(c). We remind that $\gamma_{DF} = \gamma$ in the irrotational flow model. Nevertheless, no conclusions can be made from these two discrepancies. We believe that the excitation energies could be influenced significantly by non-collective features. The situation may be similar to the one in Fig. 6(b), where 4_1 state is lower than expected for the rotor. Similarly, if the 2_2 state is lowered the resulting γ_{DF} is larger. In both cases the lowering is relative to the excitation energy of the 2_1 state.

C. Higher multipole moments

It is known that in the TBRE the probability to find a 0_{gs} state followed by either one of the states 2_1, 4_1, 6_1, or 8_1 is disproportionally large as compared to what is statistically expected. For the $(19/2)^6$ model the corresponding probabilities are 10.4%, 17.3%, 11.9% and 1.8%. In an attempt to understand this, we repeat the previous study but target the collective realizations of multipolarity $\lambda = 4$, 6, and 8. For realizations with the 0_{gs} state and with the first excited state of spin λ in Fig. 5, we consider the fractional collectivity $b(\lambda) \equiv b(E\lambda, 0_{gs} \to \lambda_1)$ and the multipole moment $q_\lambda \equiv q_\lambda(\lambda_1)$. Fig. 5 shows evidences for intrinsic shapes with deformations of higher multipolarities. In particular, for $\lambda = 4$ and 8 there is a sizable number of collective realizations where $b(\lambda) > 0.7$. These realizations
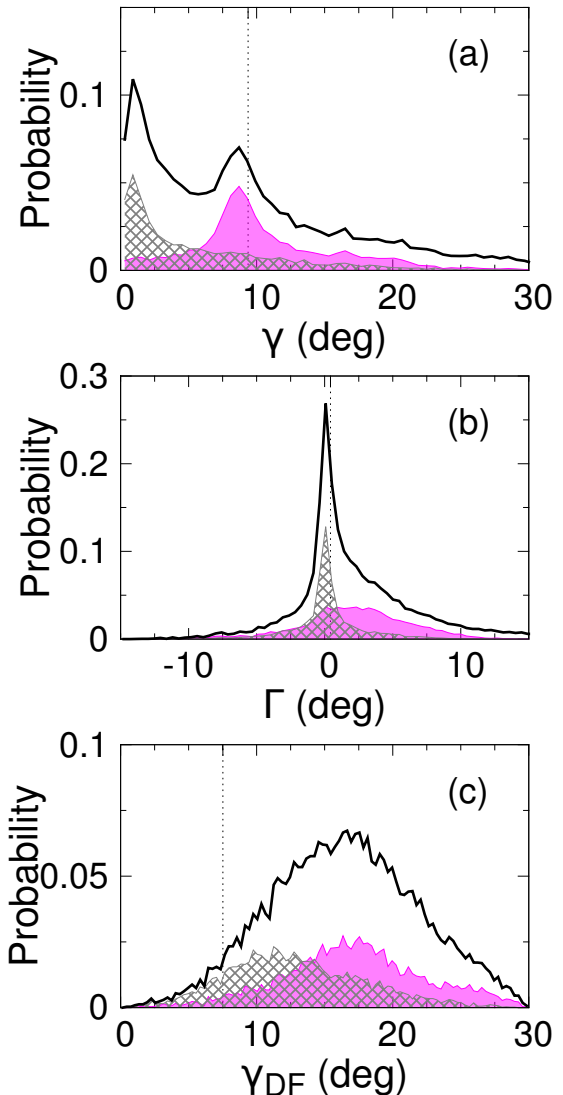

Figure 4: (Color online) $(19/2)^6$. (a) The distribution of the triaxiality angle γ . (b) The distribution of the K-mixing angle Γ. (c) The distribution of the triaxiality angle γ_{DF} from the Davydov-Filippov model. The angles are obtained from Eqs. (11), (12) and (10). We select realizations with two states of spin 2 in the spectrum and require $b > 0.7$ and $q(2_1) \approx -q(2_2)$; 18.3% of realizations satisfy this set of restrictions. The realizations with prolate and oblate shapes are shaded with the same patterns as in Figs. 2 and 3. Vertical grid lines indicate the triaxiality parameters calculated from the QQ Hamiltonian, which are: $\gamma = 9.79°$, $\Gamma = 0.73°$, and $\gamma_{DF} = 7.52°$ from Tab. I.

are shaded in red. The corresponding distributions of the multipole moments in Figs. 5(d) and 5(f) have peaks which are centered at non-zero values of q_λ. The $\lambda = 6$ shape collectivity is nearly absent in the $(19/2)^6$ system: the realizations are mostly non-collective, $b(6) < 0.7$ shaded in blue, and the corresponding moment has a peak
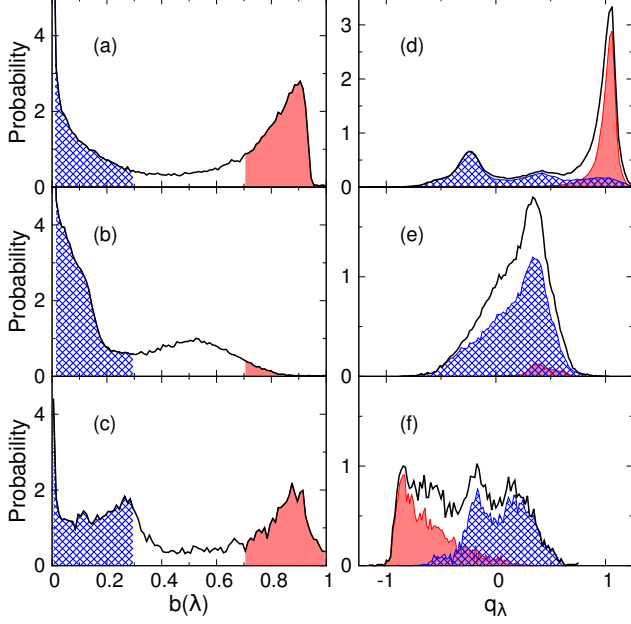
Figure 5: (Color online) $(19/2)^6$. The distributions of the fractional collectivity $b(\lambda)$ are shown in panels (a), (b), and (c). The distributions of the intrinsic multipole moments q_λ are shown in panels (d), (e), and (f). The plots are organized in three rows corresponding to multipolarities with $\lambda = 4$, 6 and 8. Here we include realizations where, in addition to the 0_{gs} state, the first excited state is either 4_1, or 6_1, or 8_1. The shaded areas correspond to collective and non-collective modes with $b(\lambda) > 0.7$ and $b(\lambda) < 0.3$ respectively. We use the same patterns as in Fig. 1.

centered near zero.

Investigations of other single j systems show presence of multipole collectivities with $\lambda = 2, 4, 6$, and 8. Generally, the collectivities corresponding to the intrinsic quadrupole shape are the most pronounced ones, however there are signatures of realizations with shapes of higher multipole deformation. The existence of such geometric structures may be related to the symmetries discussed in Ref. [11]

D. Multipole structure of the Hamiltonian

In this subsection we discuss the multipole structure of the two-body Hamiltonian in the single j level model. For this purpose we use a larger system of 8 nucleons in the same $j = 19/2$ model space, i.e. the $(19/2)^8$ model. The distributions of the fractional collectivity, the quadrupole moment, and the relative transition strength shown in Figs. 6 and 7 are similar to the distributions observed in the $(19/2)^6$ model in Figs. 1 and 2. The main difference between the models is that, in contrast to Fig. 1(b), only oblate ground state configurations are present in Fig. 6(b).

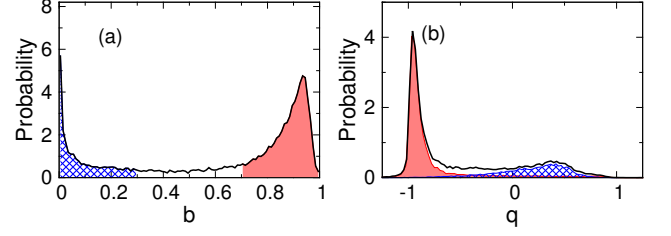The collectivities observed in the single j studies are

Figure 6: (Color online) $(19/2)^8$. The same figure as Fig. 1 but for the 8-particle system. (a) The distribution of the fractional collectivity b. (b) The distribution of the intrinsic quadrupole moment q. The histogram is comprised of 7.5% of random spectra with 0_{gs} and 2_1 states. Shaded areas correspond to 4.6% of collective realizations ($b > 0.7$) and 1.9% of non-collective realizations ($b < 0.7$). This figure is analogous to Figs. 1 and 5, and the same shading is used in these figures.
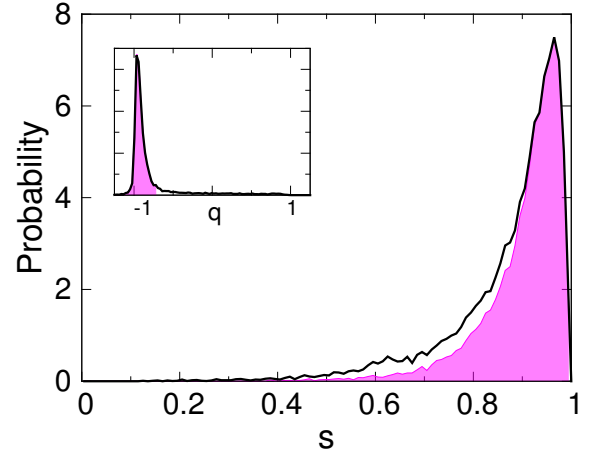

Figure 7: (Color online) $(19/2)^8$. The same figure as Fig. 2 but for the 8-particle system. The distribution of the relative transition strength rule s for the collective realizations. This figure is analogous to Fig. 2, and the same shading is used as in Figs. 2 and 3, however only oblate shapes ($q < -0.7$) are seen.

deeply rooted in the underlying geometric structure of the Hamiltonian. To focus on this relation we express the two-body Hamiltonian in the particle-hole channel in terms of the multipole operators

$$H = \sum_{\mathcal{K}} \tilde{V}_{\mathcal{K}} \sum_{\varkappa} \mathcal{M}^\dagger_{\mathcal{K}\varkappa} \mathcal{M}_{\mathcal{K}\varkappa}. \tag{13}$$

The interaction parameters $\tilde{V}_{\mathcal{K}}$ in the particle-hole channel are determined from those in the particle-particle channel V_L via Pandya transformation

$$\tilde{V}_{\mathcal{K}} = \sum_L (2L+1)\chi_L^{\mathcal{K}} V_L. \tag{14}$$

The transformation coefficients

$$\chi_L^{\mathcal{K}} = \left\{ \begin{array}{ccc} j & j & \mathcal{K} \\ j & j & L \end{array} \right\},$$

are given by the six-j recoupling coefficients.

On a single j level only even values of the particle-pair angular momenta L are allowed by the Fermi statistics. Thus, there are $j + 1/2$ interaction parameters V_L in Eq. (14). In the TBRE a set of these parameters can be viewed as a random vector in the $j + 1/2$ dimensional space. There is no such a restriction on the particle-hole momentum $\mathcal{K}$. Thus, the inverse transformation

$$V_L = \sum_{\mathcal{K}} (2\mathcal{K} + 1)\chi_{\mathcal{K}}^L \tilde{V}_{\mathcal{K}} \qquad (15)$$

may produce some unphysical V_L with odd values of L. Such Pauli-forbidden terms in the Hamiltonian do not generate any dynamics. Therefore the $2j + 1$ parameters $\tilde{V}_{\mathcal{K}}$ contain passive components which can be removed making $\tilde{V}_{\mathcal{K}}$ linearly dependent [12].

The interaction terms that correspond to the multipoles with momentum $\mathcal{K} = 0$ and $\mathcal{K} = 1$ are constants of motion [17]. The $\mathcal{K} = 0$ term in Eq. (13), describes the nucleon-nucleon interaction that is the same for all angular momentum channels, $V_L = \chi_L^0 = \text{const}$, as follows from Eq. (15). The resulting monopole Hamiltonian is proportional to the number of particle-pairs in a system. This Hamiltonian has no dynamical effect. Thus, there is no change in results if one constrains the TBRE by projecting out the monopole $\mathcal{K} = 0$ component as follows

$$V_L \rightarrow V_L - \chi_L^0 \frac{\sum_{L'}(2L' + 1)\chi_{L'}^0 V_{L'}}{\sum_{L'}(2L' + 1)\left(\chi_{L'}^0\right)^2}. \qquad (16)$$

This effectively reduces the number of independent parameters V_L.

In a single j model space the $\mathcal{K} = 1$ multipoles are proportional to the angular momentum operators $\mathcal{M}_{1\varkappa} \sim J_{\varkappa}$. Therefore the $\mathcal{K} = 1$ interaction leads to a rotational $E(J) \sim J(J + 1)$ spectrum with $\tilde{V}_{\mathcal{K}=1}$ determining the moment of inertia. In the particle-particle channel, the J^2 operator is obtained with $V_L = \chi_L^1 \sim \text{const} + L(L+1)$. Consistently, it was argued in Refs. [2, 18] that those interactions that lead to the positive moment of inertia are likely to result in the $J_{gs} = 0$. The exact J^2 operator component in the interaction can be removed by orthogonalization to χ_L^1 following the procedure in Eq. (16).

The changes in dynamics are no longer trivial when the quadrupole $\mathcal{K} = 2$ component in the interaction is modified. The role of different multipoles in the TBRE is studied in Fig. 8 and 9 where we remove different $\mathcal{K}$ components from the interaction Hamiltonian in Eq. (13) using the Graham-Schmidt projection procedure. In the particle-particle channel the projection of pairing interaction $V_L = \delta_{L,0}$ has been extensively discussed in Ref. [2]. The removal of pairing does not lead to any significant qualitative change, we thus forgo this topic in what follows.
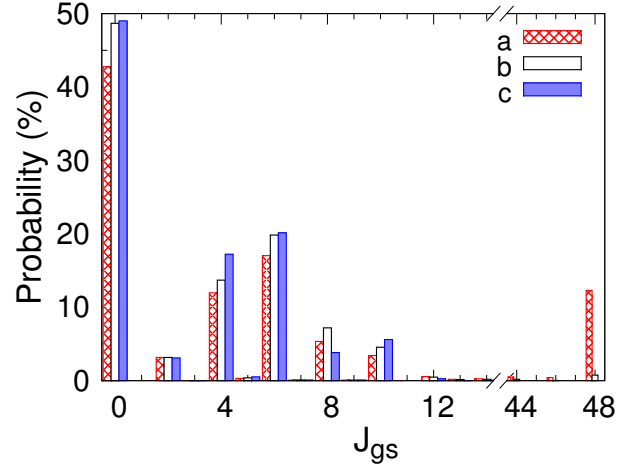

Figure 8: (Color online) $(19/2)^8$. Probabilities to observe a certain ground state spin J_{gs} for three random ensembles: (a) the TBRE, (b) the TBRE without a J^2 term (the $\mathcal{K} = 1$ term in Eq. (13) is removed), and (c) the TBRE without both, J^2 and QQ terms (the $\mathcal{K} = 1$ and $\mathcal{K} = 2$ terms in Eq. (13) are removed).

The probability to observe a certain ground state spin in the $(19/2)^8$ system is shown in Fig. 8. Three cases of random ensembles are reviewed: (a) the traditional TBRE where all $j + 1/2$ interaction parameters V_L are random Gaussian variables, (b) the case where $\mathcal{K} = 1$ term is removed, and (c) the ensemble where $\mathcal{K} = 1$ and $\mathcal{K} = 2$ multipole components are removed from the Hamiltonian. While the wave functions in ensembles (a) and (b) are identical, the ground state spin distributions are different. The role of the J^2 moment-of-inertial-like term has been discussed before in Refs. [2, 13, 18]; it appears to be fully responsible for the cases with maximum possible spin. As seen in Fig. 8, the states with the maximum spin almost never occur as ground states in ensembles (b) and (c) where the J^2 interaction term ($\mathcal{K} = 1$) is removed.

The ensembles (b) and (c) shown in Fig. 8 appears to have similar ground state spin distributions but the behavior of the fractional collectivity is different. In Fig. 9 for all three ensembles we show the distribution of the fractional collectivity of the transition between the 0_{gs} and 2_1 states. It is evident that the quadrupole collectivity disappears once the quadrupole component in the interaction is removed. Thus, we conclude that the quadrupole-quadrupole component in the interaction generates the corresponding deformation and is responsible for the rotational behavior observed.

IV. MODELS BEYOND SINGLE j

In this section we expand the scope of our models and consider systems with two single-particle levels. The richer geometry allows one to study the roles of particle-
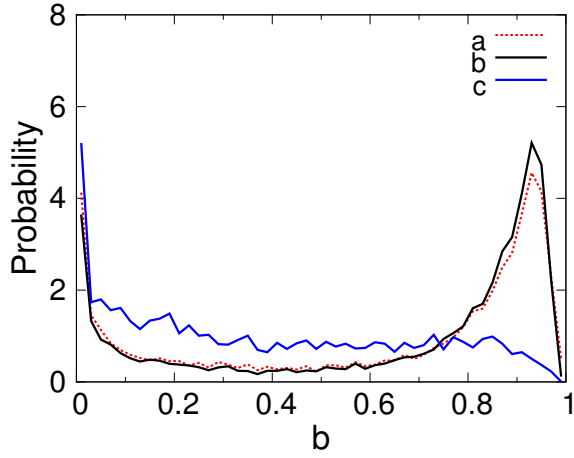
Figure 9: (Color online) $(19/2)^8$. The distribution of the fractional collectivity b for the same three random ensembles as in Fig. 8. Namely: (a) the traditional TBRE, (b) the TBRE without a J^2 term, and (c) the TBRE without both, J^2 and QQ terms. We select realizations with the 0_{gs} state followed by the first excited state 2_1. The fraction of such cases for ensembles (a), (b), and (c) is 7.6%, 8.2%, and 4.7% respectively.

hole symmetry, parity, and the structure of the multipole operators. We remind that in the TBRE the distribution of the random two-body interaction parameters is Gaussian, same unit variance is used for all symmetry classes. For models beyond single j level the nucleon pairs of a given symmetry can be constructed in several different ways. For consistency with the GOE, the variance of the off-diagonal pair-transfer matrix elements is halved as compared to the diagonal matrix elements in the two-body Hamiltonian.

The distributions of the fractional collectivity and of the quadrupole moment are shown in Figs. 10 for the $(13/2^+, 13/2^+)^6$ system. Here the model space is comprised of two levels with $j_1 = j_2 = 13/2$. Both single-particle levels have positive parity, so that the effective spherical Hartree-Fock mean-field Hamiltonian can contain terms of a mixed structure such as $a_{j_1}^\dagger a_{j_2}$. These terms are scalars for $j_1 = j_2$. There is some arbitrariness in the choice of the single-particle matrix elements of the multipole operator $\mathcal{M}_{2\mu}$ which depend on the radial overlap of the operator r^2. We choose the radial overlap to be diagonal $\langle j_1|r^2|j_1\rangle = \langle j_2|r^2|j_2\rangle$ and $\langle j_1|r^2|j_2\rangle = 0$; another possibility, with $\langle j_1|r^2|j_1\rangle = \langle j_2|r^2|j_2\rangle = \langle j_1|r^2|j_2\rangle$, has been explored and led to no substantial difference.

A structurally different $(13/2^+, 13/2^-)^6$ model is examined in Fig. 11 where two levels of equal spin and different parity are considered. In this case the matrix elements of the Hamiltonian are restricted by parity. The same structure of the quadrupole operator is used. The model space of this kind has been explored in Ref. [19] because it is the simplest model space that allows for quadrupole and octupole modes. The prevalence of the
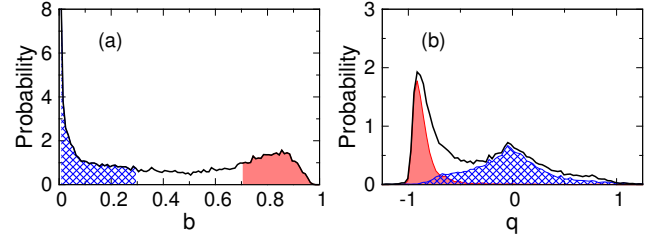

Figure 10: (Color online) $(13/2^+, 13/2^+)^6$. (a) The distribution of the fractional collectivity b. (b) The distribution of the intrinsic quadrupole moment q. The 4.1% of samples have the $0_{gs}, 2_1$ sequence. Shaded areas correspond to 1.2% of collective realization and to 1.8% of non-collective realizations. This figure is analogous to Figs. 1, 5, and 6, and the same shading is used in these figures.
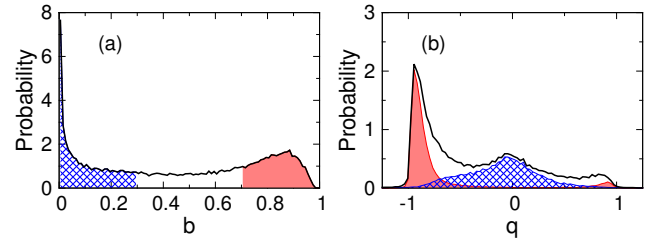

Figure 11: (Color online) $(13/2^+, 13/2^-)^6$. (a) The distribution of the fractional collectivity b. (b) The distribution of the intrinsic quadrupole moment q. The 6.9% of samples have the 0_{gs} state and the first state 2_1, both of positive parity. The 2.4% of collective and 2.6% of non-collective realizations are shaded with patterns. This figure is analogous to Figs. 1, 5, 6, and 10, and the same shading is used in these figures.

positive parity ground states is remarkable in this model. The ground state is most likely to have spin-parity 0^+, 4^+, or 24^+ with 35%, 19%, and 14% probability, respectively. In contrast, 0^-, the most probable negative parity ground state, happens only in 3% of realizations. For the $(13/2^+, 13/2^-)^6$ model the number of many-body states is the same for both parities, 8,212 each.

For both $(13/2^+, 13/2^+)^6$ and $(13/2^+, 13/2^-)^6$ models, the results related to the quadrupole collectivity are almost identical, see Figs. 10 and 11. Moreover, these results are similar to those for the single j level models, compare to Figs. 1 and 6. The major features in the distributions of b and q persist despite a bigger number of random parameters defining the Hamiltonians, more complex geometry of the two-level models, and a more chaotic resulting dynamics. There is a peak in the distribution of the fractional collectivity b near 1 indicating a sizable number of collective cases. The distribution of the quadrupole moment for the collective realizations (shaded in red) has a well-defined peak on the oblate side. The non-collective realizations appear to have quadrupole moment distribution centered at zero (shaded in blue).

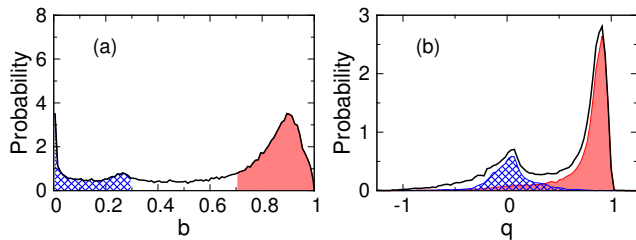For systems with exact particle-hole symmetry the

Figure 12: (Color online) $(13/2^+, 13/2^+)^{22}$. (a) The distribution of the fractional collectivity b. (b) The distribution of the intrinsic quadrupole moment q. The system is particle-hole conjugated to that in Fig. 10. The percentage of samples with the $0_{gs}, 2_1$ sequence is 8.1% which includes 4.8% of collective and 1.7% of non-collective. This figure is analogous to Figs. 1, 5, 6, 10, and 11, and the same shading is used in these figures.

Figure 13: (Color online) $(0f_{7/2}, 1p_{3/2})^8$. (a) The distribution of the fractional collectivity b. (b) The distribution of the intrinsic quadrupole moment q. The solid black line outlines the probability distribution for 31% of realizations with the 0_{gs} state followed by the 2_1 first excited state, both states with isospin $T = 0$. The 8.8% of realizations are collective and the 12.8% are non-collective. This figure is analogous to Figs. 1, 5, 6, 10-12, and the same shading is used in these figures.

quadrupole moment for particles is equal in magnitude and opposite in sign to that of holes. Moreover, characteristics such as excitation energies, spins of states, and transition rates, are exactly equal for particle-hole conjugated systems. The particle-to-hole transformation for any two-body Hamiltonian amounts to the same Hamiltonian for holes but with an additional one-body term. Thus, the symmetry is not exact in a two-level model space. Nevertheless in the TBRE, where two-body matrix elements are selected symmetrically about zero, the one-body term averages to zero. Therefore, the results in Figs. 12 and 10 for particle-hole conjugated systems $(13/2^+, 13/2^+)^{22}$ and $(13/2^+, 13/2^+)^6$ are nearly symmetric. The main difference is that the Hamiltonian for holes contains random single-particle energies which leads to a different fraction of collective realizations in the ensembles.

V. REALISTIC VALENCE SPACE

The schematic models discussed in the previous sections all seem to possess the rotational low-lying spectrum which is an evidence of the intrinsic deformation. However, to what extend they reflect the dynamics of realistic nuclei remains a question. The oblate intrinsic deformation observed in our models seems to be inconsistent with the prolate dominance in real nuclei (see discussion in Sec. VI), moreover, the semi-magic nuclei with one type of valence nucleons are generally not deformed. To attend to these issues we examine a realistic valence space consisting of the $0f_{7/2}$ and $1p_{3/2}$ single-particle levels, allowing for both protons and neutrons. The matrix element of the quadrupole operator for this model are constructed using the harmonic oscillator single-particle wave functions, we use the same effective charge for both types of nucleons. The multipole operator in this form facilitates comparison with the SU(3) group.

In Fig. 13 we present our results for the $(0f_{7/2}, 1p_{3/2})^8$ system with 8 nucleons: 4 protons and 4 neutrons. This
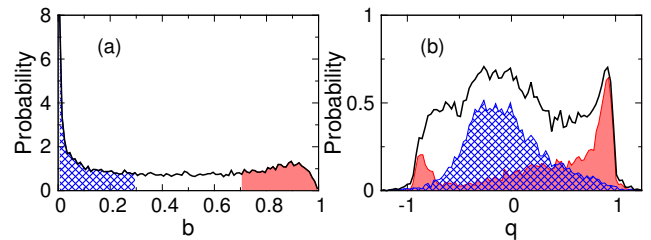
corresponds to the configuration space of ^{48}Cr nucleus. In Fig. 13(a), where the fractional collectivity b is shown, a noticeable peak that corresponds to collective realizations is observed. For the collective realizations shaded in uniform red the distribution of the quadrupole moment in Fig. 13(b) shows prolate and oblate peaks. The non-collective cases in Fig. 13(b) are distributed around $q = 0$ (shaded in blue pattern). In agreement with the results in Ref. [7], in this TBRE the prolate intrinsic shape is more probable, as evident from a bigger prolate peak.

In Fig. 14 we focus on the 8.8% of realizations that are collective. The quadrupole moments in Fig. 13(b) are further separated into prolate $q > 0.7$ and oblate $q < -0.7$ cases as shown in the inset of Fig. 14. The same shading is used in the main figure showing the distribution of the relative transition strength s. The maximum possible value $s = 1$ is reached when the ground state wave function of the randomly selected Hamiltonian coincides with that of the QQ Hamiltonian. From the summary in Tab. I one finds that the $J = 0, T = 0$ ground state of the QQ Hamiltonian, for which $s = 1$, is prolate in this valence space. Indeed, the distribution of prolate realizations is peaked at around $s = 0.8$, while the oblate shapes have s near $s = 0.6$.

The distributions of B_{42} and R_{42} for collective realizations are shown in Fig. 15. This figure can be compared to Fig. 3 for the $(19/2)^6$ system. In both figures we use the same shading to separate the prolate and oblate collective cases. In contrast to Fig. 3(a), both prolate and oblate realizations in Fig. 15(a) have a band structure with the deexcitation ratio B_{42} that is consistent with the rotational value $10/7$. This ensemble, based on the more realistic model space, appears to have an energy spectrum that is closer to the rotational spectrum. The distribution of R_{42} in Fig. 15(b) is broad, but it has a peak around the rotor value of $10/3$.

The collectivities observed in the two-body random ensemble are influenced by the single-particle level struc-
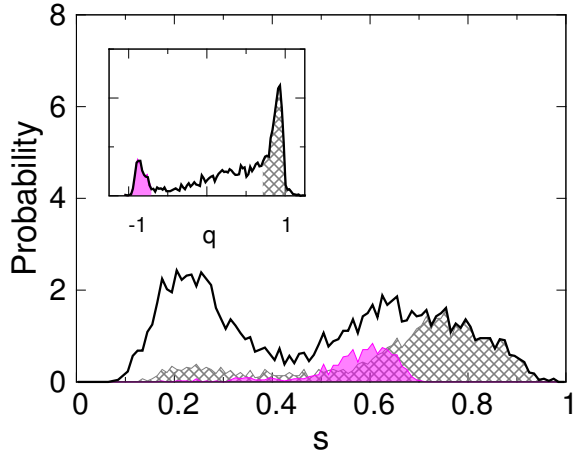
Figure 14: (Color online) $(0f_{7/2}, 1p_{3/2})^8$. The distribution of the relative transition strength s for the collective realizations (shaded with uniform red in Fig. 13). The 3.6% of prolate cases and 1.0% of oblate are identified with shades of color and pattern (see the inset). This figure is analogous to Fig. 2, and the same shading is used as in Figs. 2-4.
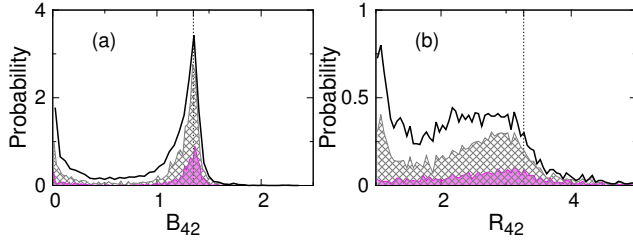

Figure 15: (Color online) $(0f_{7/2}, 1p_{3/2})^8$. (a) The distribution of the deexcitation ratio B_{42} defined in Eq. (9). (b) The distribution of the excitation energy ratio R_{42} defined in Eq. (8). Collective realization discussed in Fig. 13 are selected and, in addition, we require that the second excited state has spin 4. The fraction of such cases is 4.2%, with 2.4% being prolate and 0.6% being oblate, they are shaded separately with the same patterns as in Fig. 14. The values for B_{42} and R_{42} from the QQ Hamiltonian listed in Tab.I are shown with the vertical grid lines. This figure is analogous to Fig. 3, and the same shading is used as in Figs. 2-4 and 14.

ture which could be interpreted as a representation of the mean-field structure of the core. The presence of the shell structure may inhibit the role of the two-body Hamiltonian resulting in reduced collectivity. This effect is known in realistic nuclei and is seen in model studies including the SU(3) and seniority models for deformation and pairing. In Fig. 16 we demonstrate the effect of the core's mean-field by considering a system with the following splitting of the single-particle energies $\delta\epsilon = \epsilon_{f3/2} - \epsilon_{f7/2} = 7$. The unit of energy is determined by the variance of the two-body matrix elements, which can also be expressed in terms of the variance of the level density for the two-particle system. The results in Fig. 16 are similar to those in Fig. 13 for the degenerate
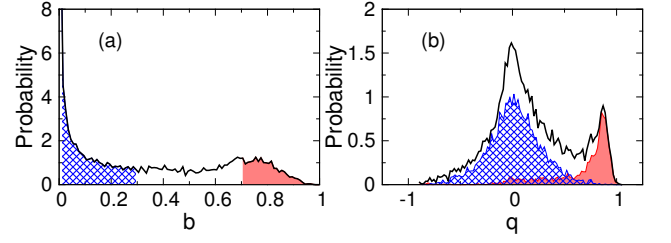

Figure 16: (Color online) $(0f_{7/2}, 1p_{3/2})^8$ with $\delta\epsilon = 7$. (a) The distribution of the fractional collectivity b. (b) The distribution of the intrinsic quadrupole moment q. The system is the same as in Fig. 13, but the single-particles energies are non-degenerate, with $\delta\epsilon \equiv \epsilon_{p3/2} - \epsilon_{f7/2} = 7$. The solid black line outlines the probability distribution for 15.7% of realizations with the 0_{gs} state followed by the 2_1 first excited state, both states with isospin $T = 0$. The 2.9% of realizations are collective and the 8.1% are non-collective. This figure is analogous to Figs. 1, 5, 6, 10-12, and 13, and the same shading is used in these figures.

model, the main difference is that the single-particle level splitting reduces the number of collective realizations by about a factor of two. Another interesting observation is that the oblate shapes no longer emerge.

As concluded in Ref. [7], realizations with rotational features appear in random ensembles due to correlated interaction matrix elements. Similarly to the single j level model, it is natural to attribute this collectivity to the QQ component in the Hamiltonian. The overlap x between the ground state wave functions of the two-body random ensemble $|0_{gs}(\text{TBRE})\rangle$ and the fixed ground state wave function of the QQ Hamiltonian is defined as

$$x = |\langle 0_{gs}(\text{TBRE})|0_{gs}(\text{QQ})\rangle|^2. \quad (17)$$

Fig. 17 shows the distribution of the overlap x in the $(0f_{7/2}, 1p_{3/2})^8$ model. A similar approach has been used in investigations of pairing coherence in random ensembles, see review in Ref. [2]. We select 56.3% of realizations where the ground state quantum numbers are $J_{gs} = 0$ and $T_{gs} = 0$; the ground state of the QQ Hamiltonian has the same spin and isospin. The distribution of x shown in Fig. 17 is compared to the Porter-Thomas χ^2 distribution. The latter emerges for uncorrelated wave functions in the 126-dimensional space spanned by the $J = 0, T = 0$ wave functions. As shown in Fig. 17 the Porter-Thomas distribution drops abruptly, thus predicting that cases with large x are extremely unlikely. According to the Porter-Thomas distribution the probability to find $x > 0.1$ is only 0.03% whereas in the TBRE $x > 0.1$ in 18.8% of random realizations. To emphasize the relation between the collective structure and the large QQ component of the wave function we show in Fig. 17 the histogram for collective realization (with states 0_{gs} and 2_1 and $b > 0.7$). It is clear that the collective transitions and rotational structure emerge when the component of the wave functions that corresponds to the eigen-
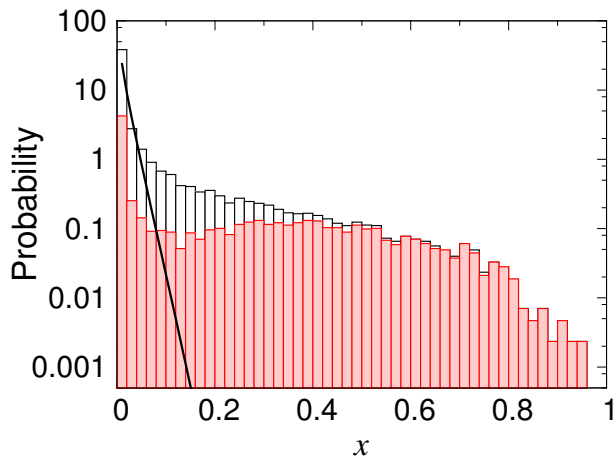
Figure 17: (Color online) $(0f_{7/2}, 1p_{3/2})^8$. The distribution of the overlap x defined in Eq. (17). The results for all $J_{gs} = 0, T_{gs} = 0$ states are unshaded; the fraction of such realizations is 56.3%. Collective realization that in addition to the 0_{gs} state have the $T = 0, 2_1$ first excited state and $b > 0.7$ are shaded (their fraction is 8.8%). Solid line shows the Porter-Thomas distribution, which is expected for the overlap between uncorrelated states.

state of the QQ Hamiltonian is large.

VI. SUMMARY

Our studies show that a collective behavior that resembles realistic is likely to be present in the ensemble with two-body random interactions. This behavior appears to emerge due to the quadrupole-quadrupole interaction component in the Hamiltonian. This component, as well as some higher multipoles, can establish some noticeable coherence despite the overall many-body randomness and complexity. Similarly to the moment-of-inertia-like J^2 term (that is responsible for the ground states with the maximum possible spin) the QQ component, while not a constant of motion, is dynamically prevailing. Let us list the supporting arguments:

- The fraction of random realizations that are quadrupole-collective is extremely large as compared to the statistically expected number.

- In the two-body random ensemble, the quadrupole collectivity displayed by the transition rates disappears when the QQ component in the interaction is removed, see Fig. 9.

- From investigations in Fig. 17, as well as indirectly form Figs. 2, 7, and 14, it follows that the collective states in the TBRE have structure similar to that of the QQ Hamiltonian eigenstates.

- The type of the quadrupole deformation and most of the quantitative measures of the QQ Hamilto-

nian summarized in Tab. I and discussed in what follows, are consistent with those observed in the TBRE. This again suggests that the collective features seen in the TBRE arise from the coherent QQ component.

In light of this finding it is instructive to examine characteristics of the deformed mean-field using the QQ Hamiltonian, for which the geometry of the configuration space is the only parameter. The values of the quadrupole moments, transition rates, level spacings, and triaxiality parameters for different models are summarized in Tab. I. In all cases the QQ Hamiltonian has a low-lying rotational spectrum; this can be seen from values of b, q, B_{42}, and R_{42}, which are close to rotational.

Using the method described in Sec. III, it is possible to discuss triaxiality in the QQ Hamiltonian. While not perfect, some features of triaxiality are identifiable. The sums of the excitation energy ratios $A = R_{2_1 3_1} + R_{2_2 3_1}$ and $B = 4R_{2_1 5_1} + R_{2_2 5_1}$ are approximately equal to 1 as expected in the triaxial-rotor model. There is a 2_2 state with a quadruple moment of comparable magnitude and of the opposite sign relative to that of the 2_1 state. For the TBRE in the $(19/2)^6$ model, the results displayed in Fig. 4 are consistent with the values of the QQ Hamiltonian in Tab. I. For the realistic model space $(0f_{7/2}, 1p_{3/2})^8$ the triaxiality in the QQ Hamiltonian is weaker, see Tab. I. The discrepancy between the magnitudes of the quadrupole moment of the 2_1 and 2_2 states points to the fragmentation of the 2_2 state. In general, the shell structure introduced by the single-particle level splitting reduces the manifestations of triaxiality and of rotational features.

Practically all deformed nuclei in nature are known to have a prolate ground state shape. This prolate dominance has been widely discussed in the literature [20–23]. An effort to pinpoint the origin of the phenomenon using the shell model approach with random interactions is presented in Ref. [7]. While in this work we do not explicitly pursue the question of prolate dominance, we are compelled to comment on the issue from the standpoint of our findings. Our studies fully confirm the results in Ref. [7]. However, conclusions supporting the prolate dominance are difficult to draw, instead we offer several observations.

First, the quadrupole collectivity seen in the TBRE is due to the QQ component in the Hamiltonian. This interaction and the geometry of the valence space determine the deformation type. Thus, some questions of the shape systematics can be addressed by considering the QQ Hamiltonian and without invoking random interactions.

Second, the shape is determined by the valence configuration and by the positions of the single-particle levels. The role of the single-particle level structure discussed by Hamamoto in Ref. [23] is possible to pinpoint using the TBRE as well as using analytic models, e.g. the seniority model and Elliot's SU(3) model [24]. For example, in our study in Fig. 16 the introduction of the single-particle

	$\delta\epsilon$	b	q	B_{42}	R_{42}	$q(2_2)$	A	B	γ(deg)	Γ(deg)	γ_{DF}(deg)
$(19/2)^6$		0.97	-0.979	1.42	3.31	0.874	1.005	1.026	9.79	0.43	7.52
$(19/2)^8$		0.95	-0.969	1.43	3.27	0.852	0.986	1.002	12.59	0.52	7.41
$(13/2^+, 13/2^+)^6$	0	0.98	-0.977	1.41	3.29						
$(13/2^+, 13/2^-)^6$	0	0.98	-0.977	1.41	3.29						
$(0f_{7/2}, 1p_{3/2})^8$	0	0.97	0.996	1.35	3.27	-0.587	1.051	1.227	4.68	-0.03	13.1
$(0f_{7/2}, 1p_{3/2})^8$	4.2	0.96	0.984	1.36	3.30	-0.387	1.031	1.460	3.34	1.83	11.77
$(0f_{7/2}, 1p_{3/2})^8$	7	0.94	0.972	1.36	3.29	-0.167	1.375	1.666	4.42	1.88	10.97

Table I: Characteristics of the QQ Hamiltonian. Listed in the table are the values of the fractional collectivity b, quadrupole moment q of the 2_1 state, ratios of the transition rates B_{42} and the excitation energies R_{42}, the quadrupole moment $q(2_2)$ of the 2_2 state, the sums of excitation energy ratios $A \equiv R_{2_1 3_1} + R_{2_2 3_1}$ and $B \equiv 4R_{2_1 5_1} + R_{2_2 5_1}$, and three triaxiality parameters γ, Γ, and γ_{DF} (see Eqs.11,12, and 10). The models are the same as those considered in our study of the TBRE. The two-level models are degenerate except for the $(0f_{7/2}, 1p_{3/2})^8$ model with $\delta\epsilon \equiv \epsilon_{p3/2} - \epsilon_{f7/2} = 4.2, 7$; the energy scale in this case is given by the variance of the level density for the two-particle system.

level splitting, that follows the realistic order, results in disappearance of oblate realizations.

Third, due to particle-hole symmetry, which does not need to be exact, the number of prolate and oblate configurations is approximately the same within a given valence space. The deviations from this symmetry affect only a few mid-shell systems where the two shapes compete. The effect of the particle-hole symmetry is seen in our results in Figs. 10 and 12.

To conclude, in this work we examined the quadrupole collectivity that emerges in systems with two-body random interactions. A low-lying spectrum, characteristic of a rigid rotor, is commonly observed. The transition $B(E2, 0_{gs} \to 2_1)$, the quadrupole moment of the 2_1 state, and the deexcitation ratio $B(E2, 4_1 \to 2_1)/B(E2, 2_1 \to 0_{gs})$ are all consistent with that of a deformed rotor. A weak triaxiality is also identified. The coherent dynamical role of the quadrupole-quadrupole interaction component is established as a source of this behavior.

[1] C. W. Johnson, G. F. Bertsch, and D. J. Dean, Phys. Rev. Lett. **80**, 2749 (1998).
[2] V. Zelevinsky and A. Volya, Phys. Rep. **391**, 311 (2004).
[3] C. W. Johnson and H. A. Nam, Phys. Rev. C **75**, 047305 (2007).
[4] T. Papenbrock and H. A. Weidenmuller, Rev. Mod. Phys. **79**, 997 (2007).
[5] Y. M. Zhao, A. Arima, and N. Yoshinaga, Phys. Rep. **400**, 1 (2004).
[6] R. Bijker and A. Frank, Phys. Rev. Lett. **84**, 420 (2000).
[7] M. Horoi and V. Zelevinsky, Phys. Rev. C **81**, 034306 (2010).
[8] J. P. Elliott, Proc. Roy. Soc. **245**, 562 (1958).
[9] R. Casten, *Nuclear structure from a simple perspective*, vol. 23 (Oxford University Press, Oxford; New York, 2000).
[10] F. Iachello and A. Arima, *The interacting boson model* (Cambridge University Press, Cambridge Cambridgeshire; New York, 1987).
[11] P. C. Huu-Tai, A. Frank, N. A. Smirnova, and P. Van Isacker, Phys. Rev. C **66**, 061302 (2002).
[12] A. Volya, Phys. Rev. C **65**, 044311 (2002).
[13] D. Mulhall, A. Volya, and V. Zelevinsky, Phys. Rev. Lett. **85**, 4016 (2000).
[14] G. Thiamova, D. J. Rowe, and J. L. Wood, Nucl. Phys. **A780**, 112 (2006).
[15] A. S. Davydov and G. F. Filippov, Nucl. Phys. **8**, 237 (1958).
[16] J. M. Allmond, R. Zaballa, A. M. Oros-Peusquens, W. D. Kulp, and J. L. Wood, Phys. Rev. C **78**, 014302 (2008).
[17] V. Zelevinsky, D. Mulhall, and A. Volya, Phys. Atom. Nucl. **64**, 525 (2001).
[18] A. Volya, Phys. Rev. Lett. **100**, 162501 (2008).
[19] V. Zelevinsky, A. Volya, and N. Auerbach, Phys. Rev. C **78**, 014310 (2008).
[20] B. Castel and K. Goeke, Phys. Rev. C **13**, 1765 (1976).
[21] B. Castel, D. J. Rowe, and L. Zamick, Phys. Lett. B **236**, 121 (1990).
[22] N. Tajima, Y. R. Shimizu, and N. Suzuki, Prog. Theor. Phys. Suppl. **146**, 628 (2002).
[23] I. Hamamoto and B. R. Mottelson, Phys. Rev. C **79**, 034317 (2009).
[24] V. Abramkina, Ph.D. thesis, Florida State University (2011).